Artifact Removal in Long-Range Single Photon LiDAR via Waveforms-Guided Depth Image Estimation

Jiying Chang, Jining Li, Rui Yu, Kai Chen, Yuye Wang, Kai Zhong, Degang Xu, and Jianquan Yao

***Abstract*—Single-photon light detection and ranging (LiDAR) has widespread applications due to the ultra-high sensitivity of the single-photon detector. However, the reconstruction has been plagued by multiple types of noise caused by crosstalk, dark counts, and background light. Artifacts produced by crosstalk are particularly difficult to distinguish directly from the signal for single photon avalanche diode (SPAD) array detector. This work proposes a waveforms-guided depth image estimation method to remove the signal artifacts effectively. Experiments show that a region of interest recognition ratio of 1.02 is achieved at 4.2 km. The study demonstrates that this waveform-guided method has excellent potential for accurate target recognition in a long range.**

***Index Terms*—Single-photon LiDAR, depth imaging, artifact removal, d-ToF.**

I. Introduction

SINGLE-PHOTON light detection and ranging (LiDAR) is a type of three-dimensional imaging LiDAR based on the principle of direct Time-of-Flight (d-ToF) of light with single-photon sensitivity which plays a key role in target tracking, medium-altitude mapping, and autonomous vehicle [1], [2], [3]. For a long time, how to suppress background noises with extremely low light level is the main problem of single-photon LiDAR (SPL) research. Recently, imaging under many unfavorable conditions, for example, atmospheric obscurant [4], fog [5], and underwater [6], has been explored and refined. Moreover, long-range imaging up to 200 km has been achieved due to the excellent imaging algorithms and system design [7]. The key problem of limiting detection distance is that the long-range echo signal reflected by the target is weak and mixed with the noise.

One approach is to optimize the system design such as adopting a narrow-band filter, adjusting the clear aperture, and adaptive gating detection to reduce noise as much as possible [7], [8], [9]. Besides, numerous photon-efficient imaging algorithms have been developed to take full advantage of the weak echo signal in addition to utilizing the system design. A classical algorithm based on penalized maximum likelihood estimation (PMLE) has been proposed by Kirmani et al. in 2014 [10]. Then a three-step procedure including reflectivity estimation, ambient noise censoring, and 3D estimation is adopted to obtain the depth image profile with a signal level of $\sim$1 photon per pixel (PPP). This approach takes full advantage of the sparse prior knowledge of the depth image. The core idea, PMLE, has been widely applied in the depth image recovery algorithms afterward [11], [12], [13]. Besides, the Bayesian approach has been introduced to adopt the prior knowledge about the interest [14], [15], [16]. It provides good estimates, but the computation time is longer compared with the previous PMLE.

The artifact noise is defined as a type of noise that accompanies the signal and is caused by multiple scattering of the signal or crosstalk of the detector arrays. Both the special system design and the photon efficiency imaging algorithm need to accumulate multiple pulses to improve the signal-to-noise ratio. The artifact noise is also accumulated as the signal is accumulated. Photon-efficient imaging algorithms achieve outstanding recovery accuracy in the photon-starved regime. However, it treats the artifact noise as a signal for some special cases. In 2022, Wu et al. proposed an intensity-guided depth imaging method to remove noise by the edge extraction of reflectivity images [17]. It encounters problems when there is a considerably different reflectivity among target surfaces. A more effective method is to identify target edges by extracting target echo signal characteristics. The waveform features are extracted by adopting the principal component analysis (PCA) method and the noise is removed by the image of target feature clustering [18]. The clustering method only gives classifications, so it is difficult to confirm which class the target belongs to especially for different scenarios. This still provides a new way of removing artifact noise.

In recent years, waveform decomposition techniques have become more and more mature with the development of full-waveform LiDAR [19]. It is prospective to extract the new target feature parameters by a mathematical model of the echo waveform for SPL. This work is committed to a new depth image restoration solution by extracting the target characteristics

Manuscript received 8 September 2023; revised 15 December 2023; accepted 18 December 2023. Date of publication 21 December 2023; date of current version 3 January 2024. This work was supported by the National Natural Science Foundation of China (NSFC) under Grant 62175182, Grant 62275193, Grant U22A20123, and Grant U22A20353. *(Corresponiding authors: Jining Li; Degang Xu.)*

The authors are with the Institute of Laser and Optoelectronics, School of Precision Instruments and Optoelectronics Engineering, Tianjin University, Tianjin 300072, China, also with the Key Laboratory of Opto-electronic Information Technology, Ministry of Education, Tianjin University, Tianjin 300072, China, and also with the Key Laboratory of Micro Opto-electro Mechanical System Technology, Ministry of Education, Tianjin University, Tianjin 300072, China (e-mail: jiningli@tju.edu.cn; xudegang@tju.edu.cn).

Digital Object Identifier 10.1109/JPHOT.2023.3345332

from the response signal. The LiDAR equation for SPL is modified based on the waveform decomposition technique in the full-waveform LiDAR. Then an adaptive threshold segmentation algorithm is used to achieve the identification of the region of interest. Finally, the depth image is reconstructed by the proposed waveform-guided depth image method. The extracted waveform features are effective in dealing with the artifact noise at a long range.

II. Observation Model

A. Scattering Model of the Target

For non-scanning LiDAR, the target is usually considered to be a point target. The number of the return signal photons is mainly related to the emitted laser pulse characteristics and the target scattering characteristics. The number of echo photons is modified as follows according to the traditional LiDAR equation [20]:

$$K_s = \frac{1}{M}\frac{\eta}{h\nu}\frac{4E_t}{\pi\theta_t^2 R^2} \times \rho A_s \times \frac{\pi D_r^2/4}{\Omega_r R^2} \times \eta_{atm}^2 \eta_{sys}, \quad (1)$$

where M is the number of pixels, η is photon detection efficiency (PDE), h is Planck's constant, ν is the frequency of light, θ_t is the emitted beam divergence full angle, R is the distance of the target, D_r is the effective aperture area of the receiving optical system, η_{atm} and η_{sys} is the transmittance of the one-way atmospheric transmittance of the laser and the optical system. These parameters are considered as the constants, which are fixed in the experiment. And there are still some other non-constant parameters such as single pulse energy E_t, the target reflectivity ρ, the target optical effective reflective area A_s, and the solid angle of the target scattering beam Ω_r, which is generally represented by π for a Lambert reflector. Then we get the number of echo photons:

$$K_S = \eta_{atm}^2 \eta_{sys} \frac{1}{M}\frac{\eta}{h\nu}\frac{D_r^2}{4\pi\theta_t^2 R^4} \times E_t \times \rho A_s \frac{4\pi}{\Omega_r}, \quad (2)$$

here the scattering cross-section σ of the target is defined as

$$\sigma = \frac{4\pi}{\Omega_r}\rho A_s. \quad (3)$$

The SPL equation can be further simplified using the scattering cross-section. Besides, the echo signals are measured in time-resolved units of the time-to-digital converter in SPL. Thus, the echo signal is discretized in time-resolved bins. The modified LiDAR equation for SPL is expressed as

$$K_s(t) = \eta_{atm}^2 \eta_{sys} \frac{1}{M}\frac{\eta}{h\nu}\frac{D_r^2}{4\pi\theta_t^2 R^4} S(t) * \sigma(t), \quad (4)$$

where the system waveform $S(t)$ is a convolution between a laser pulse and a receiver response function [21]. The system waveform $S(t)$ and target scattering properties function $\sigma(t)$ are assumed to be of the Gaussian shape. Thus, the echo signal can be regarded as a mixture of Gaussian distributions as follows [22]:

$$K_s(t) = \hat{K}\exp\left(-\frac{(t-2R/c)^2}{2s^2}\right), \quad (5)$$

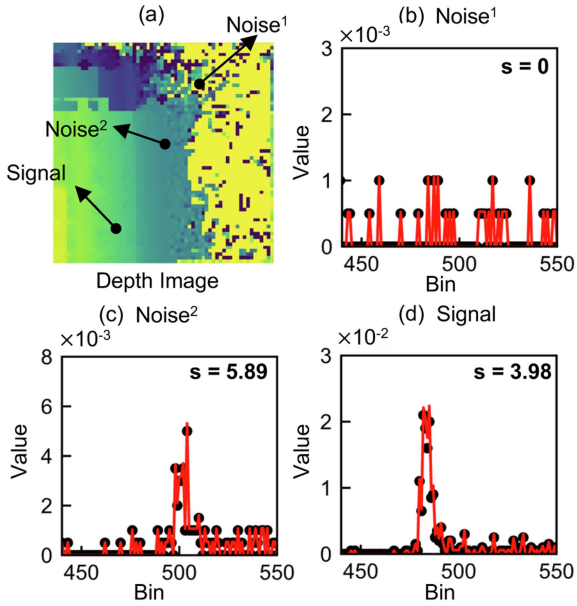

Fig. 1. (a) Depth image of the scene located at 2.2 km. (b)–(d) The photon counting histogram at pixels (10,42), (28,32) and (55,17).

where s is defined as $\sqrt{s_s^2 + s_\sigma^2}$. s_s is the standard deviation of the system waveform $S(t)$ and s_σ is the standard deviation of the scattering properties of a cluster of scatterers $\sigma(t)$.

The echo from N targets within the travel path of laser pulse is written as

$$K_s(t) = \sum_{i=1}^{N} \hat{K}_i \exp\left(-\frac{(t-2R_i/c)^2}{2s_i^2}\right). \quad (6)$$

The formula indicates that a target is regarded as a cluster of scatterers and the backscattering characteristics of the cluster of scatterers are not only related to the intensity of the measured signal but also related to the distance of the target and the standard deviation of the measured signal.

Let s be the standard deviation of the signal response. The standard deviation s from different locations is shown in Fig. 1. There are three types of returned signals. The first type of noise belongs to the background light or dark count, which is uniformly distributed throughout the detection distance gate. The second type of noise belongs to the artifact noise, which is accompanied by the signal, and its s will be larger than the signal response. But the s of target echoes is relatively constant compared with that of two types of noise and varies slightly with the characteristics of the target. This makes it possible to achieve artifact noise removal by s.

B. Detection Probability Model

One complication is that the number of primary photoelectrons K is not directly observable [10]. A relationship exists between the detection probability P of the echo signal and the number of primary photoelectrons K based on the Poisson probability response characteristics of SPL. From the process of only one trigger in each emitted pulse, the detection probability

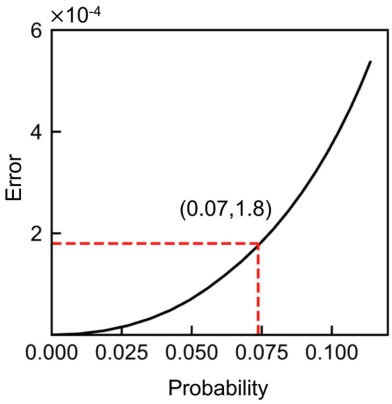

Fig. 2. Mean absolute error between the number of signal photons K_s and the detection probability against the maximum detection probability $\hat{P}$.

per interval is

$$P\left(t_{\text{bin}}\right) = e^{-\sum_{m=0}^{m=t_{\text{bin}}-1} K(m)} \left(1 - e^{-K(t_{\text{bin}})}\right), \tag{7}$$

where K represents the mean number of signal electrons occurring in the interval t_{bin}. K is the total signal photon detection K_s, dark counts K_d and background count K_b per interval.

The histogram of the detection probability shows deviations when the echo signal is strong, which is known as the saturation effect. A common method is to estimate the number of primary electrons through an observed model. Fouche et al. have shown that the detection probability varies only when the total number of primary electrons is between 0.1 and 10. This method is also not feasible when the primary electrons from the echo signal are very low. Besides, the trigger probability is obtained by accumulating multiple pulses, and the expression of the multiple-pulse probabilities of detection is more complex [23].

Here, a linear approximation between the photon number $\hat{K}$ and the detection probability $\hat{P}$ is performed at the condition of the low detection probability. This approximation is beneficial to improve the computational speed. To prove the feasibility of this linear approximation, we theoretically calculate the mean absolute error between the detection probability and the total number of primary photoelectrons K. The curves of the photoelectron number and the detection probability against the time bin are shown in Fig. 2 with the maximum signal level $\hat{K}$ varying from 0.05 to 0.20, where the standard deviation of the signal distribution is 2.626. The detection probability is approximately equal to the number of signal photons as the maximum signal level $\hat{K}$ decreases. Besides, the detection probability is calculated as 0.07 when the total number of primary electrons is 0.1. As shown in Fig. 2, the error is less than 1.8×10^{-4} when the single trigger probability is less than 0.07. Hence, the linear approximation is considered feasible. From (6), the detection probability model is expressed as

$$P_s(t) = \sum_{i=1}^{N} \hat{P}_i \exp\left(-\frac{(t - 2R_i/c)^2}{2s_i^2}\right). \tag{8}$$

The linear approximation allows us to obtain the echo signature by directly decomposing the detection probability curve. Otherwise, the total number of primary photoelectrons must be calculated using (7).

III. Data Acquisition and Reconstruction Algorithm

A. Data Acquisition

The SPL measurement system is shown in Fig. 3. The laser source (CoLID-I) is placed in parallel with the Geiger-mode avalanche photodiode detector (CETC GD5551) and triggered by a signal generator at a repetitive frequency of 20 kHz. The detector records 20,000 frames per second. Selecting more frames for reconstruction accumulates the number of signal photons in the echo signal. The 1064 nm laser has a single pulse energy of up to 125 uJ. The system configuration is detailed in our previous work [24]. In each detection cycle, the laser beam is emitted by the transmitting lens and irradiated on the target surface. Then it is diffusely reflected by the target surface. Part of the backscattering signal is collected by the receiving lens and focused on the detector. Each pixel in the detector is equipped with a timing circuit, which can record the round-trip time of the light pulse between the SPL and the target. The time-of-flight information of the photons is recorded by the computer with a timing resolution of 2 ns. The instrument response function must be longer than the time-resolved bin to measure the characteristics of the waveform. Thus, the echo waveform is obtained through multiple echo detections.

B. Reconstruction Algorithm

A novel waveform-guided depth image estimation algorithm is proposed that uses Gaussian decomposition techniques to resolve intensity, location, and variance information. The implicit assumption of Gaussian decomposition is that the cross-section profile can be represented by a series of Gaussian functions. It guides the reconstruction of depth images based on variance information. Finally, the target backscatter probability of a target scene is then derived from the reconstructed depth image. This reconstruction has the advantages of using a new target characteristic, the variance image to distinguish signal from noise, achieving a robust estimation of the target signal, and preventing artifact noise.

The reconstruction contains three parts: (i) a local gating approach to unmix signal from noise; (ii) Gaussian decomposition of the backscatter waveforms to initialize the depth image and reflectivity image; (iii) depth image and reflectivity estimation through adaptive thresholding. The photon count values of each pixel are first filtered by using spatial correlation based on a 3×3 block. The count values outside the signal width around the peak position are removed. The filtered photon count values calculate $\mathbf{T}, \mathbf{N}, \mathbf{S}$ through Gaussian decomposition pixel by pixel. The $\mathbf{T}$, $\mathbf{N}$, and $\mathbf{S}$ are the depth image, intensity image, and variance characteristics image of the target echo. For accurate decomposition, the target depth information $\mathbf{T}$ is determined by the log-matched filtering, the signal intensity $\mathbf{N}$ is determined from the count values at the peak position, and

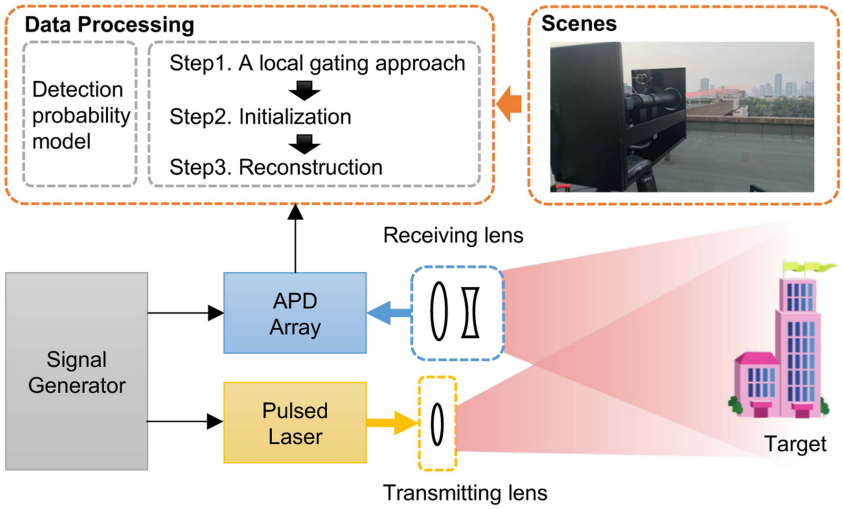

Fig. 3. Single-photon imaging set-up for the experiments.

the variance characteristics $\mathbf{S}$ of the echo signal are obtained by least squares. The region of interest (RoI) is obtained by adaptive threshold segmentation of $\mathbf{S}$. Finally, the target depth image and reflectivity image are obtained by removing the non-RoI.

The target region is defined as RoI. It is critical here to modify RoI based on the $\mathbf{S}$ image. The variance characteristics s can reflect the characteristics of the signal, as described in Fig. 1. However, the challenge is that different materials have different target scattering characteristics, which cause a fluctuant s within a certain range. The first type of noise has a smaller s, and the second type of noise has a larger s compared with the target signal. It is necessary to change the s of the second noise in order to ensure that the s of the signal echo is greater than that of the noise. Here we briefly consider subtraction. The preprocessed $\mathbf{S}$ is calculated by $\mathbf{S}' = s_0 - \mathbf{S}$, where s_0 is a constant. It is theoretically possible to select a constant larger than the s of the noise and the signal. In the experiment, it is twice the full width at half maximum signal of the transmit pulse.

The general procedure for reconstruction is listed in Algorithm 1, which completes the reconstruction process after waveform decomposition. The main difficulty is the extraction of RoI. Here, RoI is obtained by adaptive thresholding segmentation. Our main goal is to determine a suitable threshold to separate the guidance image into two parts. The ideal threshold is at the trough of the gray-level histogram of the guidance image. However, the limit between signal and noise is not apparent. We have distinguished the signal from the artifact pixel as much as possible through the preprocessing in the previous section. Finally, the optimal threshold is selected based on the discriminant criteria of the maximum between-class variance criterion [25].

Most existing schemes first utilize the time domain waveform as a priori, followed by estimating the depth information via PMLE or Bayesian estimation (BE). The waveform-guided method in this work determines whether the pixel belongs to an artifact noise response by characterizing the time domain distribution of the echo signal. The adaptive thresholding segmentation based on the variance-distributed image $\mathbf{S}$ is used to address the spurious response due to artifact noise.

Algorithm 1: Algorithm of Reconstruction.

Input: $\mathbf{T}, \mathbf{N}, \mathbf{S}$
Output: $\mathbf{D}, \mathbf{I}$
Initialize $s_0, \mathbf{D}, \mathbf{I}$
for each $i \in [0, 64)$ **do**
  for each $j \in [0, 64)$ **do**
    if $\mathbf{S}[i, j] \geq 1$ **then**
      $\mathbf{S}[i, j] = s_0 - \mathbf{S}[i, j]$
    end if
  end for
end for
$\mathbf{S} \leftarrow Medfilter2d(\mathbf{S})$
$\mathbf{S} \leftarrow MaxminNorm(\mathbf{S})$
$th \leftarrow AdaptiveThreshold(\mathbf{S})$
$\mathbf{RoI} \leftarrow th = 255$
$\mathbf{D}, \mathbf{I} \leftarrow \mathbf{T}[\mathbf{RoI}], \mathbf{N}[\mathbf{RoI}]$
return $\mathbf{D}, \mathbf{I}$

IV. Results and Analysis

Long ranges imaging at ~2.2 km and ~4.2 km away from the SPL are implemented to verify the practical capability of the proposed algorithm. The signal-to-noise ratio (SNR) decreases from 0.23 to 0.07 with the increase of distance, which leads to a decrease of accuracy. Ground truth images are calculated from 20,000 frames by the log-matched filtering method, and artifacts are also reconstructed. Finally, we obtain the accurate target edges using manual judgment and remove the artifacts.

Further, three values are used to evaluate the results, including the mean absolute error (MAE), processing time, and the ratio of the region of interest (rRoI). MAE is obtained by $\| \mathbf{D} - \mathbf{D}_{truth} \|^2 / M$. rRoI is defined as the number of pixels belonging to target regions in the reconstructed image divided

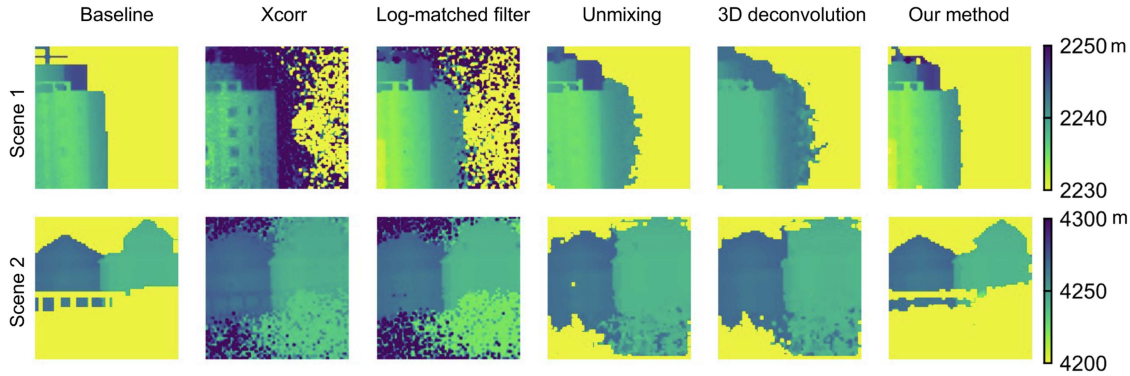

Fig. 4. Comparison of imaging results using different reconstruction methods.

TABLE I
MAE, PSNR, AND PROCESSING TIME OF DIFFERENT METHODS

Target	Method	MAE(m)	rRoI
Scene 1	Xcorr	1260.6	2.31
	Log-matched filter	1260.1	2.31
	Unmixing	257.9	1.26
	3D deconvolution	347.7	1.35
	Our method	41.1	1.02
Scene 2	Xcorr	2542.3	2.45
	Log-matched filter	2537.4	2.45
	Unmixing	1794.8	2.03
	3D deconvolution	1751.0	2.01
	Our method	129.8	1.01

by the number of pixels in the actual target region in the ground truth image, which can reflect the reconstruction algorithm's ability to recover the target region. The closer its value is to 1, the better the reconstruction result is.

Two scenes are reconstructed using different methods. Fixing the signal level equal to 95 PPP, a total of 2,000 frames is used for scene 1, and 8,700 frames are used for scene 2. The reconstructed images compared with four current classical methods: Xcorr [26], Log-matched filter [15], Unmixing [27], and 3D deconvolution algorithms [28] are shown in Fig. 4. Xcorr and the Log-matched filter method show significant enhancement of the noise, however, Unmixing and 3D deconvolution methods remove most of the noise. The waveform-guided reconstruction method accurately identifies the artifact noise by the new feature as shown in Fig. 4. The depth information of the Unmixing method is closer to the baseline depth image. However, the depth information of the waveform-guided method is closer to the Log-matched filter results because the Log-matched filter method is selected as the basic depth estimation method.

The reconstruction performance is shown in Table I. The rRoI of the waveform-guided method reaches 1.02. Besides, the MAE of the waveform-guided method outperforms others, which is decreased by 6.3 times compared with the best method among others. However, the MAE is still largely due to the system limitation. In terms of processing time, there are no advantages. The Unmixing algorithm shows a better performance thanks to the multi-threading acceleration.

Also, we compare the results of intensity-guided depth image reconstruction with those of waveform-guided image

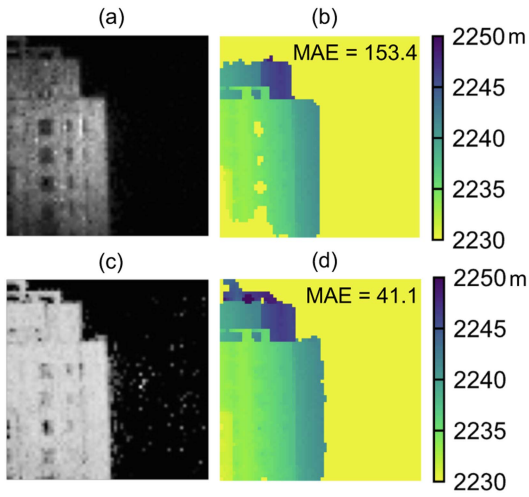

Fig. 5. Comparison with intensity-guided depth image reconstruction method. (a) Intensity-guidance image. (b) Intensity-guided reconstruction result. (c) Waveform-guidance image. (d) Waveform-guided reconstruction result.

reconstruction algorithms. Only the guidance image in the waveform-guided method is replaced, which is normalized. It can be found that $\mathbf{S}$ extracts the features of the target echo signal by comparing Fig. 5(a) and (c). There is also a small amount of noise. However, the waveform-guided reconstructed result in Fig. 5(d) is significantly better than Fig. 5(b) by adaptive threshold segmentation which decreases MAE by 3.7 times. The waveform-guided method successfully removes the false positive surface detection due to artifact noise.

Results imply that the method needs dozens of signal photons to recover the target distance due to the requirement of waveform decomposition. Another reason is that a wide instrument response function results from several undesirable factors, such as system jitter and temperature drift. The standard deviation of the instrument response function is 2.626 bin, while it is wider at long range. This results in a range error under photon-limited imaging conditions. Thus, the number of signal photons has to be increased to obtain a reliable depth estimate. We also considered waveform feature extraction using confidence intervals under fewer photons. This part of the work is still under investigation, and the feasibility remains to be ascertained.

Overall, we analyzed the performance of the waveform-guided method with a fixed signal photon level and different distances. The results show that the proposed method is effective in removing artifact noise. The processing time is longer than the multi-threaded processing. Fortunately, some procedures are able to be done in parallel, which will be considered later. The conclusion that artifact removal is feasible through the waveform-guided algorithm is not affected. The proposed method is more effective when there are stringent requirements for target identification and the ground truth image at a long range, which obviously sacrifices a portion of the imaging frame rate.

V. Conclusion

Artifacts usually appear simultaneously with the signal, which makes the reconstruction of depth images difficult. This work proposes a waveform-guided depth image reconstruction method in SPL detection that can decompose the features of the echo signal by the waveform. The recognition experiments of the target echo signal are accomplished using the feature images with two distances of 2.2 and 4.2 km. Then the performance of the waveform-guided method with a fixed signal photon level of 95 PPP and different distances is analyzed. The results show that the MAE reduces more than 13.5 times and the rRoI achieves 1.02, which demonstrates the effectiveness of this method in removing artifact noise. The waveform-guided depth image reconstruction method is a promising technology in long-range target recognition.

References

[1] Z. Li, B. Liu, H. Wang, H. Yi, and Z. Chen, "Advancement on target ranging and tracking by single-point photon counting lidar," *Opt. Exp.*, vol. 30, no. 17, pp. 29907–29922, 2022.

[2] B. R. Call, D. Kelley, D. G. Fried, C. Reichert, K. Reichel-Vischi, and A. Eldredge, "Low swap, commercially-available geiger-mode lidar system," in *Proc. SPIE*, vol. 12110, pp. 58–68, 2022.

[3] J. Taher et al., "Feasibility of hyperspectral single photon lidar for robust autonomous vehicle perception," *Sensors*, vol. 22, no. 15, 2022, Art. no. 5759.

[4] R. Tobin, A. Halimi, A. McCarthy, P. J. Soan, and G. S. Buller, "Robust real-time 3 d imaging of moving scenes through atmospheric obscurant using single-photon lidar," *Sci. Rep.*, vol. 11, no. 1, 2021, Art. no. 11236.

[5] H. Shi et al., "Noise-tolerant bessel-beam single-photon imaging in fog," *Opt. Exp.*, vol. 30, no. 7, pp. 12061–12068, 2022.

[6] H. Shi, H. Qi, G. Shen, Z. Li, and G. Wu, "High-resolution underwater single-photon imaging with bessel beam illumination," *IEEE J. Sel. Topics Quantum Electron.*, vol. 28, no. 5, Sep./Oct. 2022, Art. no. 8300106.

[7] Z.-P. Li et al., "Single-photon imaging over 200 km," *Optica*, vol. 8, no. 3, pp. 344–349, 2021.

[8] X. Zhou, J. Sun, P. Jiang, C. Qiu, and Q. Wang, "Improvement of detection probability and ranging performance of Gm-APD LiDAR with spatial correlation and adaptive adjustment of the aperture diameter," *Opt. Lasers Eng.*, vol. 138, 2021, Art. no. 106452.

[9] G. Shen, T. Zheng, Z. Li, L. Yang, and G. Wu, "Self-gating single-photon time-of-flight depth imaging with multiple repetition rates," *Opt. Lasers Eng.*, vol. 151, 2022, Art. no. 106908.

[10] A. Kirmani et al., "First-photon imaging," *Science*, vol. 343, no. 6166, pp. 58–61, 2014.

[11] D. Shin et al., "Photon-efficient imaging with a single-photon camera," *Nature Commun.*, vol. 7, no. 1, 2016, Art. no. 12046.

[12] Z.-P. Li et al., "Super-resolution single-photon imaging at 8.2 kilometers," *Opt. Exp.*, vol. 28, no. 3, pp. 4076–4087, 2020.

[13] C. Dai, W.-L. Ye, C. Yu, X. Huang, Z.-P. Li, and F. Xu, "Long-range photon-efficient 3 d imaging without range ambiguity," *Opt. Lett.*, vol. 48, no. 6, pp. 1542–1545, 2023.

[14] Y. Altmann, X. Ren, A. McCarthy, G. S. Buller, and S. McLaughlin, "Lidar waveform-based analysis of depth images constructed using sparse single-photon data," *IEEE Trans. Image Process.*, vol. 25, no. 5, pp. 1935–1946, May 2016.

[15] J. Tachella, Y. Altmann, M. Márquez, H. Arguello-Fuentes, J.-Y. Tourneret, and S. McLaughlin, "Bayesian 3D reconstruction of subsampled multispectral single-photon lidar signals," *IEEE Trans. Comput. Imag.*, vol. 6, pp. 208–220, 2020.

[16] J. Koo, A. Halimi, and S. McLaughlin, "A bayesian based deep unrolling algorithm for single-photon lidar systems," *IEEE J. Sel. Topics Signal Process.*, vol. 16, no. 4, pp. 762–774, Jun. 2022.

[17] M. Wu et al., "Intensity-guided depth image estimation in long-range lidar," *Opt. Lasers Eng.*, vol. 155, 2022, Art. no. 107054.

[18] Y. Zhang et al., "Three-dimensional imaging of ships in the foggy environment using a single-photon detector array," *Optik*, vol. 272, 2023, Art. no. 170310.

[19] S. Hancock et al., "Waveform lidar over vegetation: An evaluation of inversion methods for estimating return energy," *Remote Sens. Environ.*, vol. 164, pp. 208–224, 2015.

[20] O. Steinvall, "Effects of target shape and reflection on laser radar cross sections," *Appl. Opt.*, vol. 39, no. 24, pp. 4381–4391, Aug. 2000.

[21] C. Mallet and F. Bretar, "Full-waveform topographic lidar: State-of-the-art," *ISPRS J. Photogrammetry Remote Sens.*, vol. 64, no. 1, pp. 1–16, 2009.

[22] W. Wagner, A. Ullrich, V. Ducic, T. Melzer, and N. Studnicka, "Gaussian decomposition and calibration of a novel small-footprint full-waveform digitising airborne laser scanner," *ISPRS J. Photogrammetry Remote Sens.*, vol. 60, no. 2, pp. 100–112, 2006.

[23] D. G. Fouche, "Detection and false-alarm probabilities for laser radars that use geiger-mode detectors," *Appl. Opt.*, vol. 42, no. 27, pp. 5388–5398, 2003.

[24] J. Chang et al., "Dithered depth imaging for single-photon lidar at kilometer distances," *Remote Sens.*, vol. 14, no. 21, 2022, Art. no. 5304.

[25] N. Otsu, "A threshold selection method from gray-level histograms," *IEEE Trans. Syst., Man, Cybern.*, vol. 9, no. 1, pp. 62–66, Jan. 1979.

[26] D. Shin, J. H. Shapiro, and V. K. Goyal, "Single-photon depth imaging using a union-of-subspaces model," *IEEE Signal Process. Lett.*, vol. 22, no. 12, pp. 2254–2258, Dec. 2015.

[27] J. Rapp and V. K. Goyal, "A few photons among many: Unmixing signal and noise for photon-efficient active imaging," *IEEE Trans. Comput. Imag.*, vol. 3, no. 3, pp. 445–459, Sep. 2017.

[28] Z.-P. Li et al., "Single-photon computational 3 d imaging at 45 km," *Photon. Res.*, vol. 8, no. 9, pp. 1532–1540, 2020.